Microchimica Acta (2021) 188: 154
https://doi.org/10.1007/s00604-021-04810-4

ORIGINAL PAPER

Nanoplatform based on GSH-responsive mesoporous silica nanoparticles for cancer therapy and mitochondrial targeted imaging

Hang He[1] · Song Meng[1] · Haimin Li[1] · Qingyuan Yang[1] · Ziqiang Xu[1] · Xueqin Chen[1] · Zhengguang Sun[1] · Bingbing Jiang[1] · Cao Li[1]

Received: 30 October 2020 / Accepted: 23 March 2021 / Published online: 6 April 2021

Abstract

Mitochondria, as the energy factory of most cells, are not only responsible for the generation of adenosine triphosphoric acid (ATP) but also essential targets for therapy and diagnosis of various diseases, especially cancer. The safe and potential nanoplatform which can deliver various therapeutic agents to cancer cells and mitochondrial targeted imaging is urgently required. Herein, Au nanoparticles (AuNPs), mesoporous silica nanoparticles (MSN), cationic ligand (triphenylphosphine (TPP)), doxorubicin (DOX), and carbon nanodots (CDs) were utilized to fabricate mitochondrial targeting drug delivery system (denoted as CDs(DOX)@MSN-TPP@AuNPs). Since AuNPs, as the gatekeepers, can be etched by intracellular glutathione (GSH) via ligand exchange induced etching process, DOX can be released into cells in a GSH-dependent manner which results in the superior GSH-modulated tumor inhibition activity. Moreover, after etching by GSH, the CDs(DOX)@MSN-TPP@AuNPs can serve as promising fluorescent probe (λ_{ex} = 633 nm, λ_{em} = 650 nm) for targeted imaging of mitochondria in living cells with near-infrared fluorescence. The induction of apoptosis derived from the membrane depolarization of mitochondria is the primary anti-tumor route of CDs(DOX)@MSN-TPP@AuNPs. As a kind of GSH-responsive mitochondrial targeting nanoplatform, it holds great promising for effective cancer therapy and mitochondrial targeted imaging.

Keywords Carbon nanodots · Redox-sensitive drug delivery · Mitochondrial probe · Near-infrared fluorescence

Introduction

Fabrication of effective drug delivery systems (DDSs) is one of the most important and promising opportunities for chemotherapeutic drugs [1], making them alternative candidates to increase their utilization potentiality of chemotherapy drugs and reduce their undesired side effects. In general, the story of in vivo DDSs system to date ends with cellular internalization, great improvements, and challenges which existed in the modulation of organelle targeting [2]. On the other hand, the molecular sites of most clinically approved chemotherapeutic drugs acted on are focused on certain organelles within the specific cell [3]. Herein, targeting certain organelle within specific cells has gradually emerged as a novel attractive strategy to further increase the therapeutic efficiency.

Mitochondria, as the powerhouse inside most eukaryotic cells, are responsible for various important features, such as the conversion of energy (ATP), generation of reactive oxygen species (ROS), and especially initiation of apoptosis-associated programmed cell death [4], which implied that mitochondria are closely related to the cellular mortality managements. However, mitochondria inside cancers possess their own unique characteristics as compared to normal cells, such as hampered oxidative phosphorylation, increased glycolysis, hyperpolarization of the membrane, enhanced generation of ROS, and upregulation of antioxidant systems (glutathione (GSH))

This article is part of the Topical Collection *Nanomaterials for biomedical imaging and targeting*

✉ Ziqiang Xu
ziqiang.xu@hubu.edu.cn

✉ Cao Li
licao0415@163.com

[1] Ministry-of-Education Key Laboratory for the Green Preparation and Application of Functional Materials, Collaborative Innovation Center for Advanced Organic Chemical Materials Co-constructed by the Province and Ministry, Hubei Key Laboratory of Polymer Materials, School of Materials Science & Engineering, Hubei University, Wuhan 430062, China

[5], which show great influence on various cellular behaviors of cancer cells [6]. Moreover, such unique function and structure have made mitochondria of cancer cells more vulnerable to mitochondria active therapeutic drugs [7] which make them to be potential target sites of DDSs.

Up to now, various well-established multifunctional DDSs, such as liposomes [8], inorganic nanoparticles [9], and mesoporous silica nanoparticle (MSN)-based nanocarriers, are promising alternatives to fabricate mitochondrial targeted DDSs [10, 11]. MSN has been widely considered as promising DDSs, due to superior biocompatibility, large surface area and pore volume, superior chemical stability, and simple surface modification strategies [12].

More importantly, with the help of gatekeepers, the specific stimuli-responsive abilities can be achieved which play crucial roles in prevention of the premature release of cargos. The stimulus for the application of the MSN-based DDSs in the biosystem can come from externally introduced physical and chemical signals or biogenic chemical signals of the biosystem itself [13]. Compared with externally introduced signals, the endogenous biogenic signals are more effective and credible to fabricate MSN-based DDSs. Among various endogenous biogenic stimuli-responsive DDSs, the redox potential is especially alluring, due to the significant difference in the concentration of GSH between intracellular fluids (1–10 mM) and extracellular fluids (2–10 μM), especially the levels of cytosolic GSH in cancer cells and those in normal cells [14]. Moreover, GSH is mainly produced in mitochondria and distributed in the cytoplasm [15], so higher therapeutic efficacy can be achieved by mitochondrial targeting MSN-based DDSs. Taking this into consideration, Au nanoparticles (AuNPs), a kind of inorganic nanoparticles with superior biocompatibility which can be ruptured by ligand exchange with GSH via formation of Au-S bond to ensure drug release [16], were selected as the gatekeepers to fabricate redox-sensitive MSN-based DDSs.

On the other hand, the combination of medical therapy and bioimaging diagnostics for optimizing intracellular therapeutic efficacy and delivery behavior of MSN has emerged as an attractive field for achieving personalized medicine [17]. Herein, in order to meet the requirement of personalized medicine, the development of nanoplatform with higher loading dose and cellular imaging ability is essentially desirable. Compared with other imaging techniques, fluorescence (FL) imaging possesses numerous advantages, such as high temporal-spatial resolution and minimally invasive, especially the FL imaging in the near-infrared (NIR) window offers considerable advantages in terms of lower absorption and minimal auto-fluorescence [18]. Among various FL nanomaterials, carbon nanodots (CDs) have attracted great attention, due to unique tunable FL properties, superior biocompatibility, and easy surface modification [19, 20]. Therefore, these outstanding features make CDs promising candidates for monitoring delivery behavior of MSN with enhanced therapeutic efficiency.

Considering the unique features of MSN, mitochondrial targeting ligand (TPP), AuNPs, and CDs, it is desirable to integrate CDs and TPP with biocompatible stimuli-responsive AuNPs capped MSN to develop novel mitochondrial targeting DDSs. In this work, NIR emitting CDs are encapsulated into MSN (CDs@MSN) at first. Then mitochondrial targeting ligand triphenylphosphine (TPP) was conjugated onto MSN (CDs@MSN-TPP), and then, doxorubicin (DOX) loaded TPP-CDs@MSN were capped by AuNPs as gatekeepers (CDs(DOX)@MSN-TPP@AuNPs) to achieve redox-responsive DDSs with NIR FL imaging abilities towards cellular mitochondria to improve the therapeutic efficiency and security (Scheme 1).

Experimental section

Chemical reagents

Formamide (99%), acetonitrile (99%), hexadecyltrimethylammonium chloride (CTAC) (99%), triethylamine (TEA) (99%), and tetraethyl orthosilicate (TEOS) (99%) were purchased from Sinopharm Chem Reagent Co. (China, www.reagent.com.cn). GSH (99%), isocyanate propyl triethoxysilane (IPTS) (98%), (3-aminopropyl) triethoxysilane (APTES) (99%), and (4-carboxybutyl)triphenylphosphonium bromide (CTPB) (99%) were purchased from Aladdin Reagent Co. (China, www.aladdin-e.com). N-(3-Dimethylaminopropyl)-N′-ethylcarbodiimide hydrochloride (EDC) (98%) and N-hydroxysuccinimide (NHS) (98%) were purchased from Macklin Reagent Co. (China, www.macklin.cn). Au nanoparticles (AuNPs) were purchased from Xi'an Ruixi Biological Technology Co. (China, www.ruixibiotech.com). Dulbecco's modified Eagle medium (DMEM), fetal bovine serum (FBS), phosphate-buffered saline (PBS), and 3-(4,5-dimethylthiazol-2-yl)-2,5-diphenyltetrazolium-bromide (MTT) were purchased from Invitrogen Co. (America, www.thermofisher.com). All reagents were of analytical grade and were used as received.

Synthesis of CDs-IPTS

The bare CDs were firstly synthesized according to previous work with little modification [21]. Then, IPTS was conjugated onto the surface of CDs accordingly. Namely, 3 mg bare CDs was dissolved in 5 mL anhydrous acetonitrile; then, 60 μL IPTS was injected under the nitrogen atmosphere and they were reacted at 40 °C for 12 h to obtain CDs-IPTS. Finally, the solution was dried under a vacuum and they were directly applied for the subsequently steps.

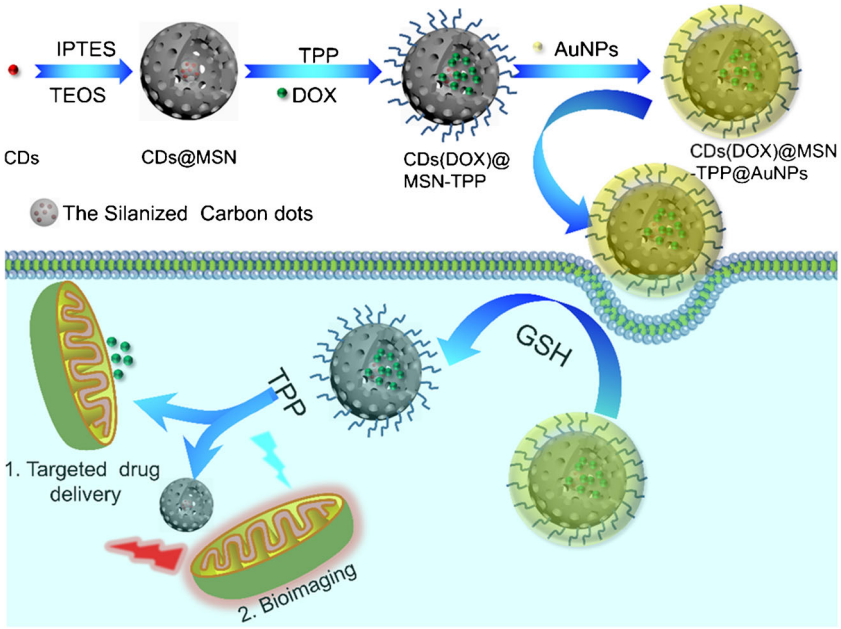

Scheme 1 The scheme for the preparation and application of CDs(DOX)@MSN-TPP@AuNPs

Results and discussions

Synthesis and characterization of CDs

Firstly, the CDs were facilely prepared via the solvothermal treatment of GSH solution in formamide according to previous work with some modification [21]. And the morphology structure, size, surface properties, and optical features were characterized and related description was presented in Electronic Supporting Materials (Fig. S1 to S4).

Synthesis and characterization of drug delivery system

In order to encapsulate the CDs into MSN, CDs should be firstly modified with silanization agent to increase their affinity with the TEOS. So IPTS with highly reactive isocyanate was covalently modified onto the surface of CDs. Compared with the FTIR spectra of CDs, additional peak centered at 1562 and 1442 cm^{-1} appeared which can be attributed to the bending vibration of N–H and C–N. This result confirmed that amino was reacted with isocyanate to form amide structure. Since the IPTS is excess, several peaks from IPTS are also in the FTIR spectra, such as $\nu_{O\text{-}H}$ between 2800 and 3000 cm^{-1}, $\nu_{N=C=O}$ at 2273 cm^{-1} and 1103 and 1079 cm^{-1} of $\nu_{Si\text{-}O\text{-}Si}$ (Fig. S5). Then, the CDs@MSN can be successfully achieved by co-hydrolyzation with TEOS in the presence of CTAC as the template [22]. After the reaction was completed, the green powder can be obtained which implied the successful encapsulation of CDs into MSN. An obvious peak at 683 nm is observed in FL spectra of the CDs@MSN which is identical to that of CDs (Fig. S6a). Another intense peak at 650 nm is observed in the rest of drug carriers, which may be caused by (de)protonation and tautomerism between the structures of -NH-C=O and -N=C-OH [23]. It also should be noted that the FL intensity of CDs@MSN-NH_2 is much higher than the rest three kinds of drug carriers, which is derived from the alkalinity of amino. Moreover, intense red FL is also observed under excitation of 405-nm light (inset of Fig. S6a). On the other hand, the XRD patterns of three types of MSN show a broad peak at 22.6° which may be referred to the interlayer spacing (002) of graphitic structure (Fig. S6b) [24].

It is very obvious that CDs@MSN were uniform and spherical with statistic size distribution of approximately 36.4 ± 15.0 nm (Fig. 1a, b and S7a). A highly uniform mesoporous network can be clearly found in the TEM images with higher magnification. After the amination reaction, uniform and spherical nanoparticles are still observed in TEM images while their statistic size distribution increases to 38.8 ± 12.5 nm (Fig. 1c, d and S7b). Moreover, the obvious mesoporous structure is still observed in the CDs@MSN-NH_2 (Fig. 1c, d). When the AuNPs were capped onto CDs@MSN-TPP, AuNPs (denoted as black dots) were found to be uniformly distributed on the exterior surface of CDs@MSN-TPP (Fig. 1e). The black dots (AuNPs) on CDs@MSN-TPP exhibited an apparent lattice spacing about 0.24 nm which can be assigned to the planar distance for Au (111) (0.235 nm) [25], proving the successful deposition of AuNPs onto the surface of CDs@MSN-TPP (Fig. 1f). The successful deposition can also be proved by the SEM-based element mapping (Fig. 1g).

Then, N_2 adsorption-desorption isotherms were applied to analyze the surface areas and pore sizes of different nanoplatforms. As shown in Fig. 1h, the N_2 adsorption-sorption isotherms of CDs@MSN imply the existence of

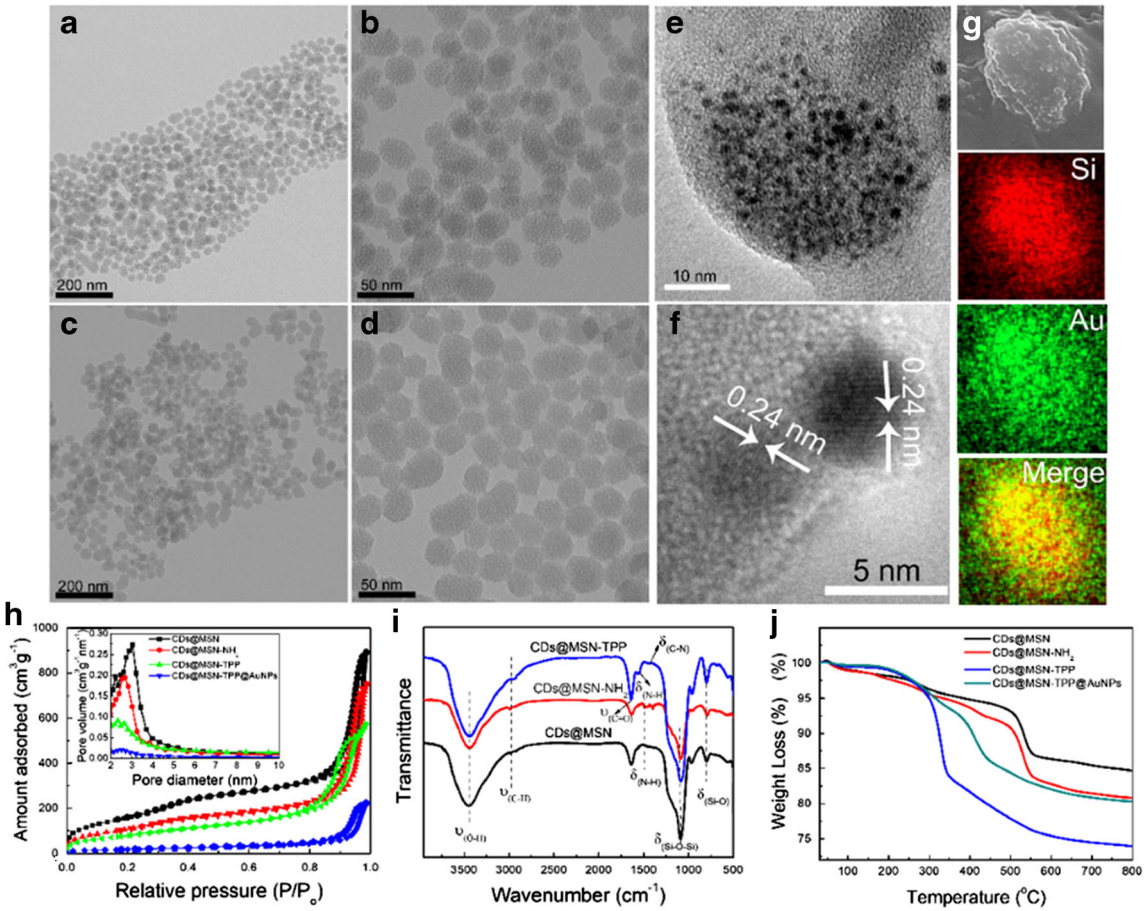

Fig. 1 The characterization of the nanoplatform. TEM images of CDs@MSN with low magnification (**a**) and high magnification (**b**). TEM images of CDs@MSN-NH_2 with low magnification (**c**) and high magnification (**d**). High-resolution images of CDs@MSN-TPP@AuNPs with low magnification (**e**) and high magnification (**f**). SEM mapping CDs@MSN-TPP@AuNPs (**g**). The nitrogen adsorption-desorption isotherms of nanoplatfrom. Inset: Barrett–Joyner–Halenda pore distribution of different nanoplatforms (**h**). The FTIR spectra of different nanoplatforms (**i**). TGA curves of different nanoplatforms (**j**)

obvious narrow wedge mesoporous structure. All the other samples exhibit similar curves to that of CDs@MSN while sharp reductions of the nitrogen adsorption capacity are observed after every step of modification which implies that the mesopores of the CDs@MSN have been blocked stepwise. And the changes of determined S_{BET}, D_{BJH}, and V_p can further confirm the successful modification of CDs@MSN (Fig. 1h and Table S1). As for each step of surface modification, their zeta surface potential varied regularly (Fig. S8).

Then, the modification process was further monitored by FTIR spectra (Fig. 1i). The bending vibration of -NH_2 at 1488 cm^{-1} proved the successful formation of CDs@MSN-NH_2. The CDs@MSN-NH_2 also revealed an additional band at 2985 cm^{-1} which is associated with the stretching vibration of -CH_3 from the alkyl chain of APTES. After the modification of TPP, the disappearance of the typical absorption band at 1488 cm^{-1} implied that the amino groups of CDs@MSN-NH_2 were completely consumed and enhancement of signal at 1633 cm^{-1} ($\nu_{C=O}$) implied the conjugation of carboxyl of TPP. Moreover, another two tiny peaks at 1556 and 1455 cm^{-1} appeared in the spectrum of CDs@MSN-TPP, which can be attributed to the bending vibration of N–H and C–N, respectively. Then, the TGA curves of nanocarrier were also measured to confirm the successful surface modification. When the temperature increased to 800 °C, the weight loss of CDs@MSN, CDs@MSN-NH_2, CDs@MSN-TPP, and CDs@MSN-TPP@AuNPs was 15.3%, 19.2%, 26.0%, and 19.7%, respectively (Fig. 1j). The continuous increase of the weight loss values for CDs@MSN-NH_2 and CDs@MSN-TPP verifies the surface coating of nanocarrier while the decrease of weight loss also confirms the successful blocking of the nanocarriers with AuNPs.

In vitro drug release

DOX is a widely applied model anti-tumor drug in this work to fabricate nanocarriers. In order to prove that the nanocarrier could not prematurely release drugs before entering into cancer cells, the in vitro drug release studies were taken at the GSH concentration of 0, 1.25, and 10 mM to imitate the redox

environment of the extracellular matrix, normal cells, and cancer cells. The LC and EE of CDs(DOX)@MSN-TPP@AuNPs were determined to be 17.6% and 44.3%, respectively.

As shown in Fig. 2a, the release rates were quite different for CDs(DOX)@MSN-TPP@AuNPs in PBS with and without GSH. In the absence of GSH, pores of CDs(DOX)@MSN-TPP@AuNPs were blocked by AuNPs via the gold-nitrogen bond, so only about 22% of DOX was released within 120 h. On the contrary, the presence of GSH results in enhanced release of loaded DOX. When the concentration of GSH was 1.25 mM, the release rate increases a little to 26% within 120 h. However, when the concentration of GSH further increased to 10 mM, burst release from nanocarriers was observed, namely approximately 43.7% DOX was released within 24 h and accumulative release amounts of the nanocarriers reach 81.5% within 120 h. Since the extracellular GSH concentration is 100–1000 times lower than that of intracellular GSH, the as-prepared nanocarriers can encapsulate most DOX before entering cells and achieve rapid intracellular release of drugs within a short time.

To verify the mechanism of GSH-responsive drug release, then the interaction between AuNPs and GSH was studied by incubating AuNPs with GSH (10 mM). As shown in Fig. 2b–e, the AuNPs are spherical and uniformly dispersed in the absence and presence of GSH while their size decreases from 5.3 to 3.3 nm after the incubation with GSH. Moreover, the presence of clear planar distance at 0.24 nm (111) further confirmed the existence of metallic Au (Fig. 2f, g). Furthermore, when the GSH was added, the hydrodynamic diameter decreases from 10.1 to 5.6 nm which is similar to the results of TEM (Fig. S9) and zeta potential increased from −7.2 to 12.8 mV. Due to the much stronger gold-sulfur bond, the original AuNPs can be etched by GSH via ligand exchange process to form GSH capped AuNPs with a much smaller size [26]. Herein, the GSH-responsive drug release can be achieved by the above GSH induced ligand exchange induced etching process. The morphology of the nanocarriers after incubating with GSH has also been studied (Fig. S10); it is apparent that much fewer AuNPs were decorated on the surface of AuNPs and their size decreases obviously, which further proves the mechanism and feasibility of AuNPs as GSH-responsive gatekeepers.

Biocompatibility and in vitro cytotoxicity

Firstly, the cytotoxicity of pure drug nanocarriers without encapsulation of DOX was measured to prove that the drug carriers are biocompatible. In this work, three kinds of cell lines (4T1, Hela, and MCF-7) were applied as the models for the MTT assay. As shown in Fig S11, the CDs@MSN-TPP@AuNPs presented little cytotoxicity to the three kinds of cells, and the cellular viability remains over 90% within the concentration range between 0.16 and 100 μg/mL.

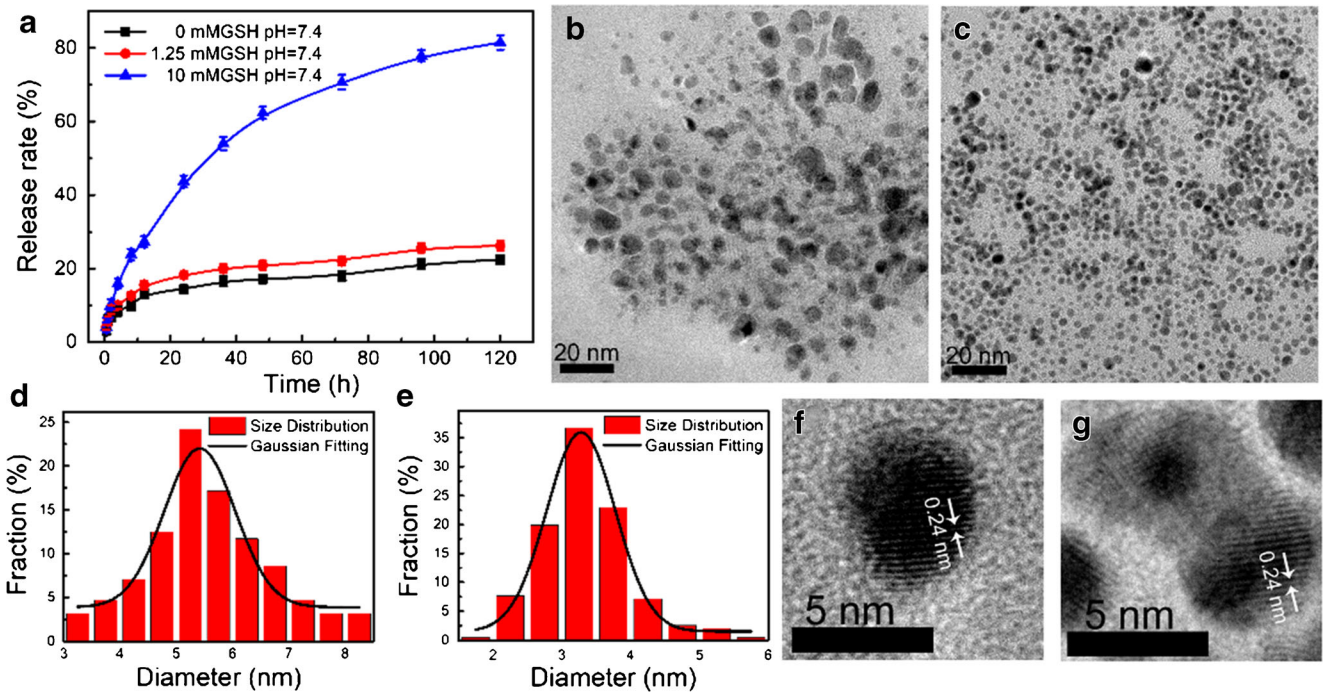

Fig. 2 In vitro drug release and their related mechanism. **a** Cumulative release of DOX from CDs(DOX)@MSN-TPP@AuNPs nanocarrier in PBS (pH = 7.4) with different GSH concentrations (0, 1.25, and 10 mmol/L) in shaking table at 37 °C. Data are shown as mean ± SD, $n = 3$ per treatment. TEM images of AuNPs before (**b**) and after (**c**) incubating with GSH. The size distribution of AuNPs before (**d**) and after (**e**) incubating with GSH. The high-resolution images of AuNPs before (**f**) and after (**g**) incubating with GSH

Table 1 IC_{50} values (μg/mL) of nanocarriers in different cell lines

Sample	IC_{50} ($\mu g \cdot mL^{-1}$)		
	Hela	MCF-7	4T1
DOX	0.88	1.00	0.55
CDs(DOX)@MSN-TPP@AuNPs	1.53	1.61	0.71
CDs(DOX)@MSN-TPP@AuNPs with BSO			6.66
CDs(DOX)@MSN-TPP@AuNPs with GSH-OEt			0.53

Subsequently, these three types of cell lines were applied to investigate the in vitro anti-cancer capability of DOX-loaded drug nanocarriers. As shown in Fig. 3 and Table 1, after three kinds of cells were co-incubated with CDs(DOX)@MSN-TPP@AuNPs at different DOX concentrations, the cell viabilities decreased obviously with the concentration of DOX increasing up to 10 μg/mL. Even though the concentration of DOX is merely 0.63 μg/mL, around 60% of Hela cells and MCF-7 were still alive while only 50% of 4T1 cells were alive. When the content of DOX increased to 5 μg/mL, about 70% Hela, 72% MCF-7, and 76% 4T1 were eliminated, which was similar to that of pure DOX. However, each pure DOX group displayed the highest anti-cancer activity, namely the IC_{50} value was around twofold lower than them against these three types of cells, which is caused by the gradual release of DOX from the drug-loaded nanocarriers [27].

Then, the GSH responsiveness of CDs(DOX)@MSN-TPP@AuNPs in the intracellular environment was investigated by co-incubating 4T1 cells as model cells with GSH-OEt and BSO which can increase and decrease the concentration of intracellular GSH, respectively [28]. Since BSO is reported to reduce the GSH level in the cell, the IC_{50} value of CDs(DOX)@MSN-TPP@AuNPs in cells pretreated with BSO was about 9.4 times higher than that of cells without any pretreatment (Fig. 3 and Table 1). Meanwhile, the IC_{50} value of cells without any pretreatment is 1.4 time higher than that of cells pretreated with GSH-OEt, which confirmed that GSH accelerates the etching of AuNPs on the surface of CDs(DOX)@MSN-TPP@AuNPs resulting in faster leakage of DOX. Herein, GSH-dependent cytotoxicity is observed in this nanoplatform which is mainly derived from the promotion/inhibition of the synthesis of GSH by pretreating with GSH-OEt/BSO [29].

Intracellular drug release

The intracellular GSH concentration regulation abilities of BSO and GSH-OEt were applied to investigate the redox-sensitive release of DOX by CLSM and flow cytometry. The result of CLSM is presented in Fig. 4. The position of the nucleus was stained by hochest33342 ($\lambda_{ex} = 405$ nm, $\lambda_{em} = 461$ nm) with blue FL. As shown in Fig. 4, red FL with different intensity ($\lambda_{ex} = 488$ nm, $\lambda_{em} = 575$ nm) was observed

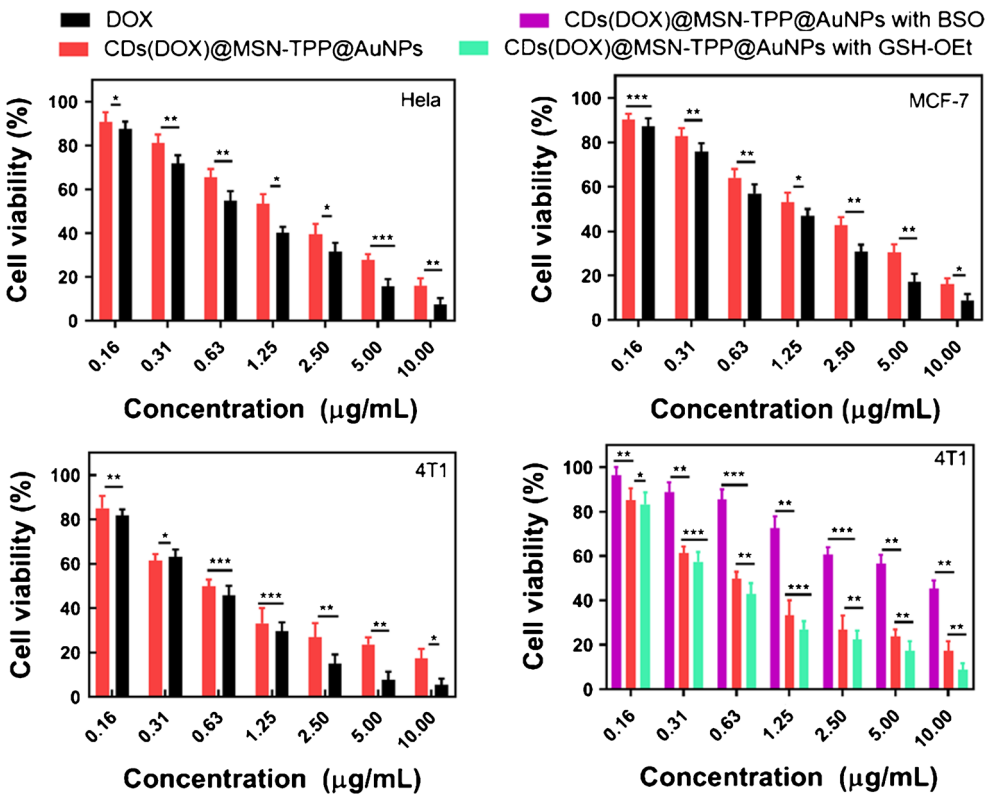

Fig. 3 In vitro cellular cytotoxicity and GSH-responsive in vitro cellular drug release. **a** Cell viabilities of HeLa, MCF-7, and 4T1 cells co-incubated with DOX and CDs(DOX)@MSN-TPP@AuNPs. And the cell viabilities of 4T1 co-incubated with CDs(DOX)@MSN-TPP@AuNPs, CDs(DOX)@MSN-TPP@AuNPs pretreated with BSO, and CDs(DOX)@MSN-TPP@AuNPs pretreated with GSH-OEt. Data shown as mean ± SD, $n = 6$ per treatment, $^{*}p < 0.05$, $^{**}p < 0.01$, $^{***}p < 0.001$

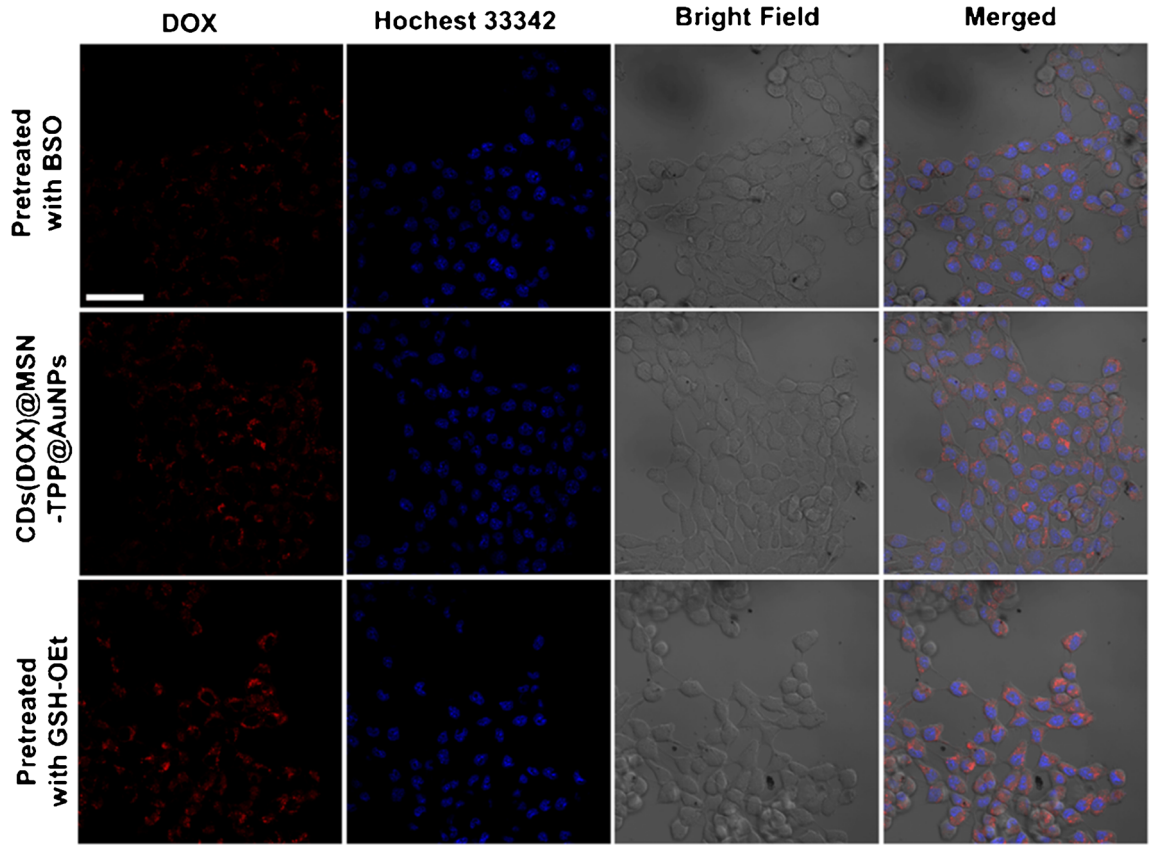

Fig. 4 CLSM images of 4T1 cells co-incubated with CDs(DOX)@MSN-TPP@AuNPs, CDs(DOX)@MSN-TPP@AuNPs pretreated with BSO, and CDs(DOX)@MSN-TPP@AuNPs pretreated with GSH-OEt. The red fluorescence is related to the signal of DOX and the nucleus of cells was stained with blue emissive Hochest33342. Scale Bar: 50 μm

insides three kinds of samples, including cells pretreated with BSO/GSH-OEt or without any pretreatment. Compared with cells without any pretreatment, much less DOX release was observed inside 4T1 cells pretreated with BSO while a much more apparent red signal was found in cytoplasm of 4T1 cells pretreated with GSH-OEt which confirm the redox-sensitive intracellular drug release of CDs(DOX)@MSN-TPP@AuNPs. On the other hand, the GSH-dependent anti-tumor activity of the nanocarrier can be verified by the bright field image of three samples. As shown in the bright field image, compared with the cells without any pretreatment, almost all the cells pretreated with BSO adhere to the confocal dish with regular morphology. However, the amounts of cells with impaired morphology and coarse surface enhanced obviously for cells pretreated with GSH-OEt (Fig. 4).

In order to quantitatively investigate the GSH-dependent cellular drug release from CDs(DOX)@MSN-TPP@AuNPs and analyze more cells to make the result more meaningful, the 4T1 cells pretreated with BSO/GSH-OEt or without pretreatment were analyzed by flow cytometry ($\lambda_{ex} = 488$ nm, $\lambda_{em} = 575$ nm) (Fig. S12). As expected, the release of DOX from nanocarrier inside cells without any pretreatment was apparently higher than that pretreated with BSO while the intracellular release of the drug further increased obviously for GSH-OEt-treated cells. Then, mean FL intensity (MFI) value was applied quantitatively to analyze the drug release behavior (Fig. S12b). The MFI value of cells pretreated with GSH-OEt was about 2.02 times higher than that without any pretreatment and 3.12 times higher than that pretreated with BSO. Combined with the above results, we can conclude that the intracellular GSH concentration plays an important role in the redox-dependent DOX release behavior via the etching of AuNPs which contribute to the GSH-sensitive anti-tumor activity.

Mitochondria targeted imaging

In order to test the feasibility of CDs(DOX)@MSN-TPP@AuNPs targeted to mitochondria, CLSM images of 4T1 cells incubated with nanoplatform were taken. After the AuNPs were etched by intracellular GSH around mitochondria in cells, then the surface TPP would be exposed which would deliver the nanocarrier to mitochondria. As shown in Fig. 5a–e, green FL related to the mitochondria stained with Mito-Tracker Green ($\lambda_{ex} = 488$ nm, $\lambda_{em} = 516$ nm), a commercially available mitochondria dyes, red signal corresponds to CDs ($\lambda_{ex} = 633$ nm, $\lambda_{em} = 680$ nm) and blue FL indicates

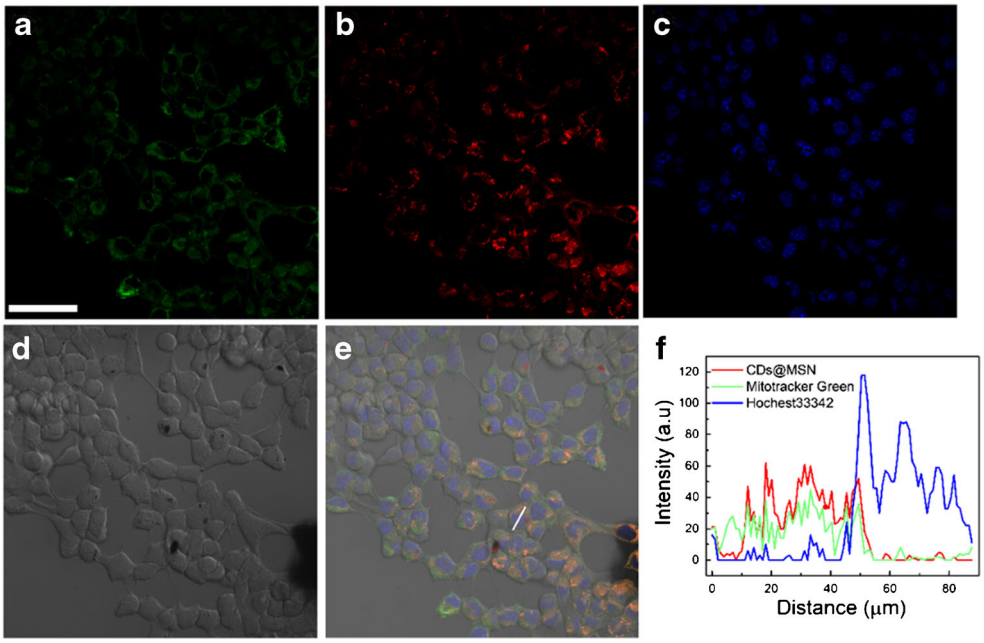

Fig. 5 Colocalization study of CDs(DOX)@MSN-TPP@AuNPs nanoplatform with mitochondria. **a** Images of green channels are related to the signal of Mito-Tracker Green which indicated the position of mitochondria. **b** Images of red channels are related to the signal of CDs. **c** Images of blue channels are related to the signal of Hochest33342 which indicated the position of nucleus. **d** Bright-field images of 4T1 cells. **e** Merged images of 4T1 cells. **f** Colocalization analysis of CDs(DOX)@MSN-TPP@AuNPs in 4T1 cells. Scale bar: 50 μm

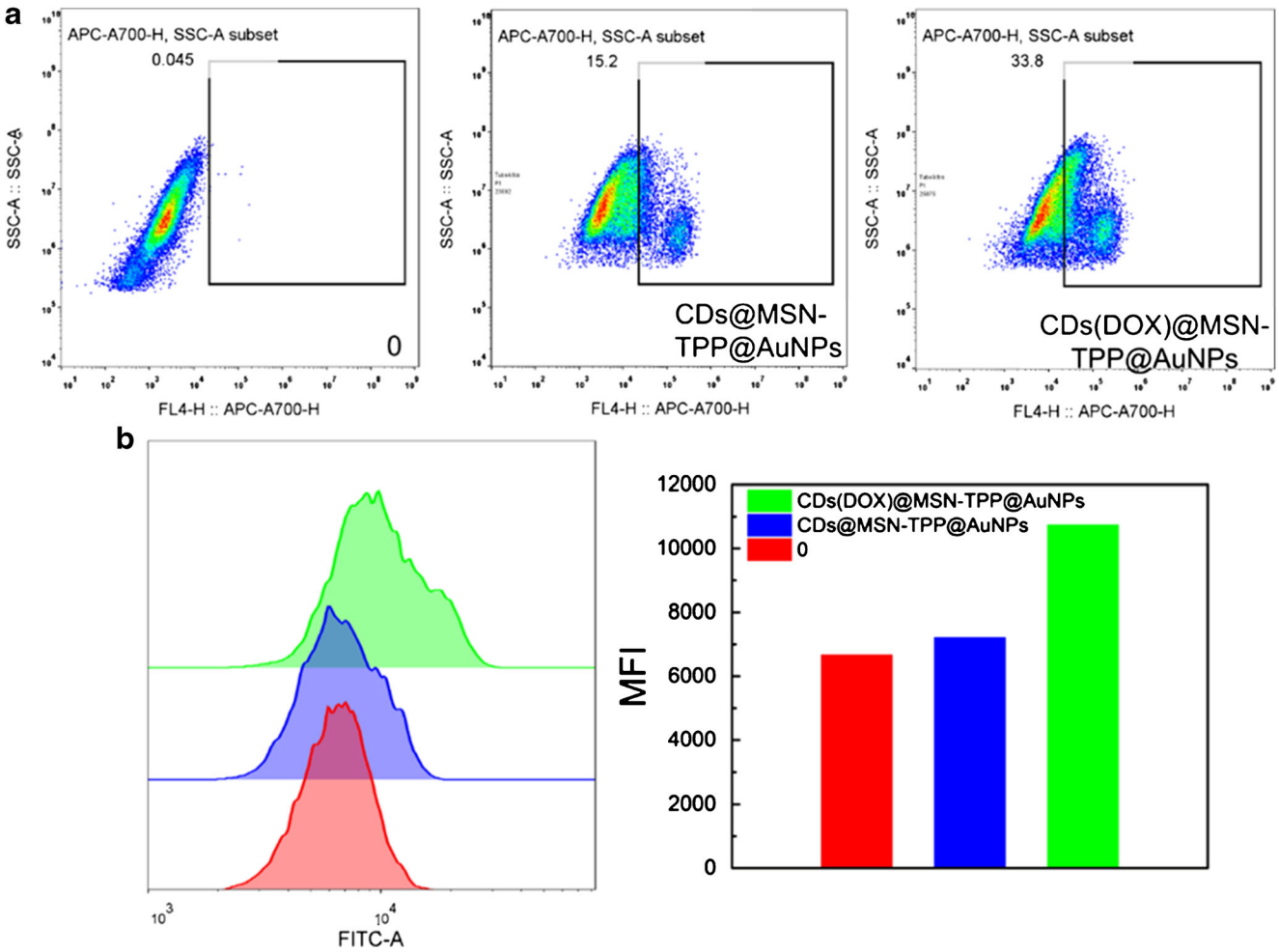

Fig. 6 In vitro anti-cancer mechanism analysis. **a** Flow cytometry analysis of cellular apoptosis of 4T1 co-incubated with CDs@MSN-TPP@AuNPs and CDs(DOX)@MSN-TPP@AuNPs. The cells were stained with annexin V-APC. **b** Flow cytometry analysis and related mean fluorescence intensity (MFI) value of 4T1 cells co-incubated with CDs@MSN-TPP@AuNPs and CDs(DOX)@MSN-TPP@AuNPs. The signal of MFI is derived from the fluorescence of Rh123

the nuclei (λ_{ex} = 405 nm, λ_{em} = 461 nm). The red FL (CDs) overlapping with green FL (mitochondria) generates numerous orange signals. The images suggest that the nanocarriers can escape from the lysosomes and selectively accumulate into the cellular mitochondria of living cells. Another colocalization analysis was utilized to analyze the targeting of the nanocarrier to the mitochondria. As for the merged images in Fig. 5e, the corresponding FL intensity profiles across the white line (indicated in CLSM images) are presented in Fig. 5f, which confirmed the superior colocalization of the green and red signals. Then, Pearson's correlation coefficients (R_r) derived from ImageJ were determined to be 0.59 which is higher than 0.50. The colocalization coefficients confirmed the good performance of CDs@MSN(DOX)-TPP@AuNPs in targeting mitochondria [30], due to the presence of cationic TPP. In general, the nanocarrier CDs(DOX)@MSN-TPP@AuNPs is an ideal fluorescent probe for targeted imaging of mitochondria in living cells. In order to evaluate the practicability of this nanoplatform, the comparison with other previous works is listed in Table S2. It indicated that this nanoprobe has superior drug loading efficiency and commendable imaging ability. Because of NIR emissive features of the CDs, the cells can be imaged with low auto-fluorescence.

Cellular anti-tumor mechanism

Since apoptosis, a programmed cell death route, is a general mode for eliminating cancer cells in cancer nano-therapy with distinct advanced anti-cancer activity [31], the treated cells were stained with annexin V-APC (λ_{ex} = 633 nm, λ_{em} = 660 nm) to investigate whether the cell death is via the route of apoptosis or not. In general, the annexin V combines with exposed phosphatidylserine on the surface in the early stage of apoptosis. As shown in Fig. 6a, the blank nanocarrier induced slight apoptosis for 4T1 cells (15.2%), indicating their high biocompatibility which is consistent with MTT assay. Furthermore, the fraction of apoptotic cell (33.8%) increased obviously when DOX was loaded in CDs@MSN-TPP@AuNPs which further proved superior anti-cancer activity of the CDs@MSN-TPP@AuNPs.

Since the nanocarrier can selectively accumulate in mitochondria in living cells (Fig. 5) and the structure and functions of mitochondria are highly related to the initiation of apoptosis-associated programmed cell death [32]. Then, the changes of mitochondrial membrane potential (MMP) were analyzed by the fluorescent probe (JC-1). The JC-1 exhibits potential dependent accumulation in mitochondria and the membrane depolarization is indicated as a decrease in the FL intensity ratio of red/green signal [33]. As shown in Fig. S13, the cells exposed to CDs@MSN-TPP@AuNPs show a comparable FL intensity ratio of red/green signal to that of the control group (λ_{ex} = 488 nm, λ_{em} = 525 nm for green signal and λ_{ex} = 488 nm, λ_{em} = 575 nm for red signal). Not surprisingly, the cell treated with CDs(DOX)@MSN-TPP@AuNPs results in a very bright green signal and negligible red FL which proved the decrease of MMP which is caused by the increasing of the mitochondria membrane's permeability. The alteration of MMP can also be confirmed by flow cytometry via fluorescent dye Rh123, as a mitochondrial specific dye, which can present quantitative information (Fig. 6b, b). Compared with 4T1 cells only stained with Rh123 (λ_{ex} = 488 nm, λ_{em} = 525 nm), the MFI value of cells incubated with CDs@MSN-TPP@AuNPs remains almost constant (from 6670 to 7213) while that of cells co-incubated with CDs(DOX)@MSN-TPP@AuNPs further increases to 10,737. As expected, the enhancement of MFI value confirmed the decrease of MMP, owing to the membrane depolarization, which implied the initial and irreversible step of apoptosis [34]. These results confirmed that the CDs(DOX)@MSN-TPP@AuNPs kill the cancer cells via the loss of MPP which contributes to the induction of cellular apoptosis.

Conclusions

In conclusion, a novel type of GSH-responsive mitochondrial targeted DDSs, named as CDs(DOX)@MSN-TPP@AuNPs, can realize redox-responsive DDSs and targeted imaging of mitochondria in living cells to improve the therapeutic efficiency and security. In vitro experiments demonstrated that DOX can be released into cells in a GSH-dependent manner which contributes to the superior GSH-modulated tumor inhibition activity. We have found that the GSH-sensitive cytotoxicity is derived from the GSH induced ligand exchange induced etching process towards AuNPs. Interestingly, based on the cationic TPP, the CDs(DOX)@MSN-TPP@AuNPs can selectively accumulate into the cellular mitochondria of living cells with bright FL. The anti-cancer mechanism of CDs(DOX)@MSN-TPP@AuNPs is via the induction of apoptosis derived from the membrane depolarization of the mitochondria. However, the anti-cancer activity of nanoplatform is not comparable to other advanced anti-cancer techniques. Herein, more novel anti-tumor strategies, such as photodynamic therapy, photothermal therapy, and chemodynamic therapy, should be combined with the mitochondrial targeting functions to fabricate more efficient anti-tumor nanoplatform.

Supplementary Information The online version contains supplementary material available at https://doi.org/10.1007/s00604-021-04810-4.

Funding This work received financial support from the National Natural Science Foundation of China (22073025, 21603067) and Hubei Nature Science Foundation of China (2019CFB748).

Compliance with ethical standards

Conflict of interest The authors declare that they have no competing interests.

References

1. Ping Y, Guo J, Ejima H, Chen X, Richardson JJ, Sun H, Caruso F (2015) pH-responsive capsules engineered from metal–phenolic networks for anticancer drug delivery. Small 11(17):2032–2036
2. Huang JG, Leshuk T, Gu FX (2011) Emerging nanomaterials for targeting subcellular organelles. Nano Today 6(5):478–492
3. Torchilin VP, Khaw B-A, Weissig V (2002) Intracellular targets for DNA delivery: nuclei and mitochondria. Somat Cell Mol Genet 27(1):49–64
4. Xu Z, Chen X, Sun Z, Li C, Jiang B (2019) Recent progress on mitochondrial targeted cancer therapy based on inorganic nanomaterials. Mater Today Chem 12:240–260
5. Indran IR, Tufo G, Pervaiz S, Brenner C (2011) Recent advances in apoptosis, mitochondria and drug resistance in cancer cells. Biochim Biophys Acta 1807(6):735–745
6. Jones D (2008) End of the line for cannabinoid receptor 1 as an anti-obesity target? Nat Rev Drug Discov 7(12):961–962
7. Galluzzi L, Larochette N, Zamzami N, Kroemer G (2006) Mitochondria as therapeutic targets for cancer chemotherapy. Oncogene 25(34):4812–4830
8. Yingchoncharoen P, Kalinowski DS, Richardson DR (2016) Lipid-based drug delivery systems in cancer therapy: what is available and what is yet to come. Pharmacol Rev 68(3):701–787
9. Cheng R, Feng F, Meng F, Deng C, Feijen J, Zhong Z (2011) Glutathione-responsive nano-vehicles as a promising platform for targeted intracellular drug and gene delivery. J Control Release 152(1):2–12
10. Qu Q, Ma X, Zhao Y (2016) Anticancer effect of α-tocopheryl succinate delivered by mitochondria-targeted mesoporous silica nanoparticles. ACS Appl Mater Interfaces 8(50):34261–34269
11. Qu Q, Ma X, Zhao Y (2015) Targeted delivery of doxorubicin to mitochondria using mesoporous silica nanoparticle nanocarriers. Nanoscale 7(40):16677–16686
12. He Q, Shi J (2014) MSN anti-cancer nanomedicines: chemotherapy enhancement, overcoming of drug resistance, and metastasis inhibition. Adv Mater 26(3):391–411
13. Chen M, He X, Wang K, He D, Yang S, Qiu P, Chen S (2014) A pH-responsive polymer/mesoporous silica nano-container linked through an acid cleavable linker for intracellular controlled release and tumor therapy in vivo. J Mater Chem B 2(4):428–436
14. Yang G, Chen C, Zhu Y, Liu Z, Xue Y, Zhong S, Wang C, Gao Y, Zhang W (2019) GSH-activatable NIR nanoplatform with mitochondria targeting for enhancing tumor-specific therapy. ACS Appl Mater Interfaces 11(48):44961–44969
15. Jomova K, Vondrakova D, Lawson M, Valko M (2010) Metals, oxidative stress and neurodegenerative disorders. Mol Cell Biochem 345(1):91–104
16. Hong R, Han G, Fernández JM, B-j K, Forbes NS, Rotello VM (2006) Glutathione-mediated delivery and release using monolayer protected nanoparticle carriers. J Am Chem Soc 128(4):1078–1079
17. Zheng M, Liu S, Li J, Qu D, Zhao H, Guan X, Hu X, Xie Z, Jing X, Sun Z (2014) Integrating oxaliplatin with highly luminescent carbon dots: an unprecedented theranostic agent for personalized medicine. Adv Mater 26(21):3554–3560
18. Mu J, Lin J, Huang P, Chen X (2018) Development of endogenous enzyme-responsive nanomaterials for theranostics. Chem Soc Rev 47(15):5554–5573
19. Xu Z, Liu Y (2021) The behavior of carbonized polymer dots at the nano-bio interface and their luminescent mechanism: a physical chemistry perspective. Chin J Chem 39:265–273
20. Huang Q, Lin X, Li F, Weng W, Lin L, Hu S (2015) Synthesis and applications of carbon dots. Prog Chem 27(11):1604–1614
21. Pan L, Sun S, Zhang L, Jiang K, Lin H (2016) Near-infrared emissive carbon dots for two-photon fluorescence bioimaging. Nanoscale 8(39):17350–17356
22. Liu C, Bao L, Tang B, Zhao J-Y, Zhang Z-L, Xiong L-H, Hu J, Wu L-L, Pang D-W (2016) Fluorescence-converging carbon nanodots-hybridized silica nanosphere. Small 12(34):4702–4706
23. Zhang S, Xiao C, He H, Xu Z, Wang B, Chen X, Li C, Jiang B, Liu Y (2020) The adsorption behaviour of carbon nanodots modulated by cellular membrane potential. Environ Sci Nano 7(3):880–890
24. Miao X, Qu D, Yang D, Nie B, Zhao Y, Fan H, Sun Z (2018) Synthesis of carbon dots with multiple color emission by controlled graphitization and surface functionalization. Adv Mater 30(1): 1704740
25. He W, Kim H-K, Wamer WG, Melka D, Callahan JH, Yin J-J (2014) Photogenerated charge carriers and reactive oxygen species in ZnO/Au hybrid nanostructures with enhanced photocatalytic and antibacterial activity. J Am Chem Soc 136(2):750–757
26. Lu Y, Chen W (2012) Sub-nanometre sized metal clusters: from synthetic challenges to the unique property discoveries. Chem Soc Rev 41(9):3594–3623
27. Wan L, Chen Z, Deng Y, Liao T, Kuang Y, Liu J, Duan J, Xu Z, Jiang B, Li C (2020) A novel intratumoral pH/redox-dual-responsive nanoplatform for cancer MR imaging and therapy. J Colloid Interface Sci 573:263–277
28. Liu J, Chang B, Li Q, Xu L, Liu X, Wang G, Wang Z, Wang L (2019) Redox-responsive dual drug delivery nanosystem suppresses cancer repopulation by abrogating doxorubicin-promoted cancer stemness, metastasis, and drug resistance. Adv Sci 6(7): 1801987
29. Zhang M, Liu J, Kuang Y, Li Q, Chen H, Ye H, Guo L, Xu Y, Chen X, Li C, Jiang B (2016) "Stealthy" chitosan/mesoporous silica nanoparticle based complex system for tumor-triggered intracellular drug release. J Mater Chem B 4(19):3387–3397
30. Zinchuk V, Grossenbacher-Zinchuk O (2009) Recent advances in quantitative colocalization analysis: focus on neuroscience. Prog Histochem Cytochem 44(3):125–172
31. Ponraj T, Vivek R, Paulpandi M, Rejeeth C, Nipun Babu V, Vimala K, Anand K, Sivaselvam S, Vasanthakumar A, Ponpandian N, Kannan S (2018) Mitochondrial dysfunction-induced apoptosis in breast carcinoma cells through a pH-dependent intracellular quercetin NDDS of PVPylated-TiO2NPs. J Mater Chem B 6(21):3555–3570
32. Friedman JR, Nunnari J (2014) Mitochondrial form and function. Nature 505(7483):335–343
33. Zhang X, Yan Q, Mulatihan DN, Zhu J, Fan A, Wang Z, Zhao Y (2018) Pharmaceutical micelles featured with singlet oxygen-responsive cargo release and mitochondrial targeting for enhanced photodynamic therapy. Nanotechnology 29(25):255101
34. Thangam R, Sathuvan M, Poongodi A, Suresh V, Pazhanichamy K, Sivasubramanian S, Kanipandian N, Ganesan N, Rengasamy R, Thirumurugan R, Kannan S (2014) Activation of intrinsic apoptotic signaling pathway in cancer cells by Cymbopogon citratus polysaccharide fractions. Carbohydr Polym 107:138–150